



## Full length article

# Martensite to austenite reversion in a high-Mn steel: Partitioning-dependent two-stage kinetics revealed by atom probe tomography, *in-situ* magnetic measurements and simulation

I.R. Souza Filho <sup>a, b, \*</sup>, A. Kwiatkowski da Silva <sup>b</sup>, M.J.R. Sandim <sup>a</sup>, D. Ponge <sup>b</sup>, B. Gault <sup>b</sup>, H.R.Z. Sandim <sup>a</sup>, D. Raabe <sup>b</sup>

<sup>a</sup> Lorena School of Engineering, University of Sao Paulo, 12602-810, Lorena, SP, Brazil

<sup>b</sup> Max-Planck-Institut für Eisenforschung, MPIE, D-40237, Düsseldorf, Germany



## ARTICLE INFO

## Article history:

Received 5 July 2018

Received in revised form

16 December 2018

Accepted 23 December 2018

Available online 27 December 2018

## Keywords:

Austenite reversion

High-Mn steel

Atom probe tomography

Thermo-kinetic simulations

Curie temperature

## ABSTRACT

Austenite ( $\gamma$ ) reversion in a cold-rolled 17.6 wt.% Mn steel was tracked by means of dilatometry and *in-situ* magnetic measurements during slow continuous annealing. A splitting of the  $\gamma$ -reversion into two stages was observed to be a result of strong elemental partitioning between  $\gamma$  and  $\alpha'$ -martensite during the low temperature stage between 390 and 575 °C. Atom probe tomography (APT) results enable the characterization of the Mn-enriched reversed- $\gamma$  and the Mn-depleted remaining  $\alpha'$ -martensite. Because of its lower Mn content, the reversion of the remaining  $\alpha'$ -martensite into austenite takes place at a higher temperature range between 600 and 685 °C. APT results agree with partitioning predictions made by thermo-kinetic simulations of the continuous annealing process. The critical composition for  $\gamma$ -nucleation was predicted by thermodynamic calculations (Thermo-Calc) and a good agreement was found with the APT data. Additional thermo-kinetic simulations were conducted to evaluate partitioning-governed  $\gamma$ -growth during isothermal annealing at 500 °C and 600 °C. Si partitioning to  $\gamma$  was predicted by DICTRA and confirmed by APT. Si accumulates near the moving interface during  $\gamma$ -growth and homogenizes over time. We used the chemical composition of the remaining  $\alpha'$ -martensite from APT data to calculate its Curie temperature ( $T_{\text{Curie}}$ ) and found good agreement with magnetic measurements. These results indicate that elemental partitioning strongly influences not only  $\gamma$ -reversion but also the  $T_{\text{Curie}}$  of this steel. The results are important to better understand the thermodynamics and kinetics of austenite reversion for a wide range of Mn containing steels and its effect on magnetic properties.

© 2018 Acta Materialia Inc. Published by Elsevier Ltd. All rights reserved.

## 1. Introduction

During the last decades, high-Mn steels have received increasing attention for automotive applications due to the possibility of car-body weight reduction without compromising crash-worthy properties [1–5]. These steels combine high strength and outstanding ductility by activating complex strain-hardening mechanisms such as planar dislocation glide, transformation-induced plasticity (TRIP), and twinning-induced plasticity (TWIP) [6]. With regard to the TRIP effect, metastable austenite ( $\gamma$ ) is prone

to transform into hcp  $\epsilon$ - and/or bcc  $\alpha'$ -martensites [7–9]. In this context, excellent strain hardening rates are observed due to a two-stage TRIP effect ( $\gamma \rightarrow \epsilon \rightarrow \alpha'$ ), for which  $\epsilon$ -martensite acts as an intermediate phase for  $\alpha'$ -formation [10–13]. Additionally, nucleation of strain-induced  $\alpha'$ -martensite (SIM) is also observed at intersections of phase regions and defects such as  $\epsilon$ -martensite, mechanical twins, stacking faults and shear bands [14–18].

Advanced Mn-based steel variants have also been designed by means of precipitation reactions, grain refinement [5], and grain boundary segregation engineering [19]. The absence of pronounced anisotropy in both mechanical properties and crystallographic textures are among the advantages of strengthening by grain refinement [20]. This can be achieved by austenite reversion ( $\alpha' \rightarrow \gamma$ ) treatments, as reported for austenitic high-Mn TRIP steels [20,21]. In this scenario, Mn diffusion plays a key role since it

\* Corresponding author. Lorena School of Engineering, University of Sao Paulo, 12602-810, Lorena, SP, Brazil.

E-mail address: [isnaldi.filho@usp.br](mailto:isnaldi.filho@usp.br) (I.R. Souza Filho).

exhibits very low diffusivity in austenite with a diffusion constant of  $D_{\gamma} = 5.89 \times 10^{-24} \text{ m}^2\text{s}^{-1}$  [22]. The high Mn diffusivity in  $\alpha'$ -martensite ( $D_{\alpha'} = 7.56 \times 10^{-21} \text{ m}^2\text{s}^{-1}$ ), however, creates a Mn flux into the growing austenite. As a result, strong partitioning and segregation effect can occur at  $\alpha'/\gamma$  interfaces and grain boundaries [22].

The complex interplay of elemental redistribution and the associated thermodynamics and kinetics of the reversion from  $\alpha'$  into  $\gamma$  on the one hand [23–25] and the importance of this transformation for a variety of steels on the other hand [26–29] have thus served as motivation for the present study. In order to observe these phenomena in a well-controlled manner and at the same enable tracking the reversion by a variety of probes including magnetism, dilatometry, microstructure and atom probe tomography we conducted slow continuous annealing treatments. In this case the development and influence of elemental partitioning can be well studied during  $\gamma$ -reversion, particularly in Fe-Mn alloys owing to the high difference in Mn diffusion between the two phases [30]. At slow heating rates, long-range diffusional processes favor matrix partitioning into solute-rich (e.g. Mn) and solute-depleted zones. In this case, Mn-enriched and depleted regions are observed to be reversed austenite and remaining  $\alpha'$ , respectively. Due to lower amounts of solute in the remaining  $\alpha'$ , its transformation to austenite is delayed to higher temperatures. Therefore, a splitting of the  $\gamma$ -reversion into two stages is clearly observed under such annealing conditions.

$\gamma$ -reversion during slow continuous annealing has been reported to proceed in different kinetic steps in maraging steels [31,32], binary and ternary alloys such as Fe-Mn/Fe-Mn-Pd [30]. In all these studies, however, the initial martensitic microstructures from which the  $\gamma$ -reversion proceeds were of lath-type, obtained by quenching. Here, we evaluate austenite reversion for strain-induced martensite in a 17.6Mn-TRIP steel. For this purpose, the steel was cold-rolled up to 80% of thickness reduction ( $\epsilon = 1.56$ ). Slow annealing treatments were conducted using both continuous dilatometry and *in-situ* magnetic probing up to 800 °C. Further interrupted dilatometry was also performed at intermediate stages of  $\gamma$ -reversion. The microstructure was characterized by high-resolution electron backscatter diffraction (EBSD). Chemical gradients between austenite and martensite for representative samples were investigated by atom probe tomography (APT) [19,22,33–35]. The experimental data were compared with thermo-kinetic and thermodynamic simulations, using DICTRA and Thermo-Calc, respectively. The growth of austenite during isothermal annealing was also evaluated by combining thermo-kinetic simulations with APT results. In a recent work, Dastur et al. [36] evaluated the Mn partitioning in an 18 wt.% Mn steel by tracking changes of the Curie temperature ( $T_{\text{Curie}}$ ) of  $\alpha'$ -martensite. Here we use the elemental partitioning observed by APT and predicted by simulation to calculate  $T_{\text{Curie}}$  of the 17.6Mn-TRIP steel. The results were comparable to the  $T_{\text{Curie}}$  values observed experimentally by means of *in-situ* magnetic measurements. This result shows that the ferromagnetic behavior of the  $\alpha'$ -martensite is linked to its elemental partitioning (viz. Mn, Al, and Si) which takes place during austenite reversion.

## 2. Experimental procedures

### 2.1. Material and cold rolling

Table 1 shows the chemical composition of the investigated steel. The as-received material was a fully-recrystallized 7-mm-thick plate, mainly composed of austenite ( $\gamma$ ) and relatively small amounts of athermal  $\epsilon$ - and  $\alpha'$ -martensite. The as-received material was rolled to an equivalent logarithmic strain ( $\epsilon$ ) of 1.56 (or 80% of

**Table 1**

Chemical composition of the studied steel expressed in terms of both wt.% and at.%.

	Mn	Si	Al	C	N
wt.%	17.6	3.22	1.71	0.042	0.014
at.%	16.9	6.1	3.4	0.19	0.05

thickness reduction) in multiple passes at room temperature.

### 2.2. Slow continuous annealing (dilatometry and *in-situ* magnetic measurements)

#### 2.2.1. Dilatometry experiments

For dilatometry, samples were cut from the 80% cold-rolled steel with dimensions of  $10 \times 1.5 \times 5 \text{ mm}^3$ , with the largest dimension ( $L_0 = 10 \text{ mm}$ ) taken parallel to the rolling direction (RD). The relative changes in length of the material ( $\frac{\Delta L}{L_0}$ ) were tracked using a Linseis L75 Platinum dilatometer. Annealing was conducted from room temperature up to temperatures of 505, 660, and 800 °C. In all treatments, heating and cooling rates were 0.05 °C/s and -0.05 °C/s, respectively. All experiments were performed under argon atmosphere.

#### 2.2.2. *In-situ* magnetic measurements

Additionally, samples from the 80% cold-rolled steel were also cut with dimensions of approximately  $5 \times 1.5 \times 1 \text{ mm}^3$  (with the 5 mm dimension//RD). Using the same protocol as the one used for dilatometry (Section 2.2.1), the samples were annealed up to 800 °C in a Vibrating Sample Magnetometer (VSM – Lakeshore, model 7404), under argon atmosphere ( $\leq 3 \text{ ppm}$  humidity and  $\leq 1 \text{ ppm}$  of  $\text{O}_2$ ). Both, heating and cooling processes were conducted in the presence of an external magnetic field of 90 Oe, applied parallel to the RD.

### 2.3. Isothermal annealing at 600 °C

For isothermal annealing experiment, one additional sample with dimensions of approximately  $5 \times 1.5 \times 1 \text{ mm}^3$  was taken from the 80% cold-rolled steel and annealed at 600 °C for 5 min under argon atmosphere.

### 2.4. Microstructural characterization

All samples were ground and polished with silica suspension (100–200 nm). For microstructural characterization, the samples were evaluated using a JEOL-6500F field-emission scanning electron microscope (SEM) coupled with an electron backscatter diffraction (EBSD) system (EDAX Hikari). High-resolution EBSD maps were acquired with a step size of 50 nm. Confidence index (CI) standardization procedure was adopted as a cleanup protocol. Furthermore, data points with CI lower than 0.1 were removed from the maps.

### 2.5. Thermodynamic and thermo-kinetic simulations

Based on the chemical composition of the steel (Table 1), stability of the phases in thermodynamic equilibrium was calculated using Thermo-Calc in conjunction with the database TCFE9 [37–39]. Additionally, the diffusion-controlled phase transformation was simulated using DICTRA in conjunction with the mobility database MOBFE4 [40–42].

### 2.6. Atom probe tomography (APT)

APT measurements were performed for the sample subjected to

dilatometry interrupted at 505 °C and for the sample isothermally annealed at 600 °C for 5 min. Needle-shape specimens were prepared for APT using a FEI Helios 600i dual-beam FIB/SEM. For extraction of the specimens, a FIB lift-out method was adopted as reported in Ref. [43]. All specimens were mounted on Si micro-tips and sharpened by annular ion milling. APT was performed on a LEAP 5000 XS straight flight path instrument for highest reconstruction accuracy at 60 K in laser-pulse mode operated at 40 pJ pulse energy. The wavelength, pulse and detection rates of the laser were 355 nm, 500 kHz and 1.5 ions detected on average per 100 pulses, respectively. For data reconstruction and evaluation, the Cameca IVAS<sup>®</sup> analysis software was used following the protocol reported by Geiser and co-authors [44].

### 3. Experimental results

#### 3.1. Microstructural characterization of the as-received and $\varepsilon = 1.56$ steels

Fig. 1 (a) and (b) show EBSD maps of the as-received and 80% cold-rolled materials, respectively. For the as-received condition, fully-recrystallized  $\gamma$ -grains are noticed, partially subdivided by athermal  $\varepsilon$ -plates. Small  $\alpha'$ -martensite laths are also found, only within the  $\varepsilon$ -martensite regions. In a preceding study, the amounts of  $\gamma$ ,  $\varepsilon$ , and  $\alpha'$  for the as-received material were determined as being 0.87, 0.11, and 0.02 respectively [45]. The 80% cold-rolled ( $\varepsilon = 1.56$ ) material is mainly composed of elongated strain-induced  $\alpha'$ -martensite (SIM) grains which are parallel to the RD. Traces of remaining  $\varepsilon$ -martensite could also be indexed for this condition, as shown in Fig. 1 (b).

#### 3.2. Slow continuous annealing

##### 3.2.1. Dilatometry experiments

Starting from the 80% cold-rolled state, the stability of the  $\alpha'$ -

martensite was evaluated during slow continuous annealing. The relative changes in length  $\frac{\Delta L}{L_0}$  of the cold-rolled material as a function of temperature are shown in Fig. 2 (a). The corresponding derivative curve over the course of the heating process is depicted in Fig. 2 (b). Fig. 2 (a) reveals two contraction events, indicating that the  $\alpha' \rightarrow \gamma$  transformation splits into two distinct stages [46,47]. Consequently, two negative peaks are observed in the derivative  $-\frac{d(\frac{\Delta L}{L_0})}{dT}$ , viz. at 505 and 660 °C (Fig. 2 b). For both stages of the  $\gamma$ -reversion, the starting ( $A_S$ ) and finishing ( $A_f$ ) temperatures were determined as those values where  $\frac{\Delta L}{L_0}$  deviates from linearity. Therefore, the first stage of  $\gamma$ -reversion starts and finishes at  $\sim 390$  ( $A_S^{1st-stage}$ ) and  $\sim 575$  °C ( $A_f^{1st-stage}$ ), respectively. By using the same approach for the second stage of  $\gamma$ -reversion,  $A_S^{2nd-stage}$  and  $A_f^{2nd-stage}$  are, respectively,  $\sim 600$  and  $\sim 685$  °C. Fig. 2 shows that the first stage of  $\gamma$ -reversion extends over a broader temperature range when compared to the second one. Additionally, the observed magnitude of contraction is smaller for the second stage. Similar results were reported by Mozsner et al. [30] for binary Fe-Mn alloys containing 5 and 10 wt.% Mn.

##### 3.2.2. In-situ magnetic measurements

The magnetization ( $M$ ) of the material during heating (red curve) and cooling (blue curve) is reported in Fig. 3 (a). The corresponding derivative  $\frac{dM}{dT}$  during the heating stage is displayed in Fig. 3 (b). Fig. 3 (a) reveals that the magnetization of the material starts to decrease at  $\sim 375$  °C. From this temperature on, the ever-decreasing values of  $M$  reach a maximum rate at 505 °C, as clearly evidenced by the first peak (at 505 °C) in the  $\frac{dM}{dT}$  curve (Fig. 3b). Such loss in magnetization with temperature can be firstly attributed to relaxation of the magneto-crystalline constants [48]. However, the main reason for such behavior is the reduction in volume fraction of the ferromagnetic phase ( $\alpha'$ -martensite), i.e. the progressing  $\gamma$ -reversion. Besides, these results agree well with dilatometric measurements (Fig. 2 b). As shown in Fig. 3 (a), the magnetization continuously decreases for higher temperatures

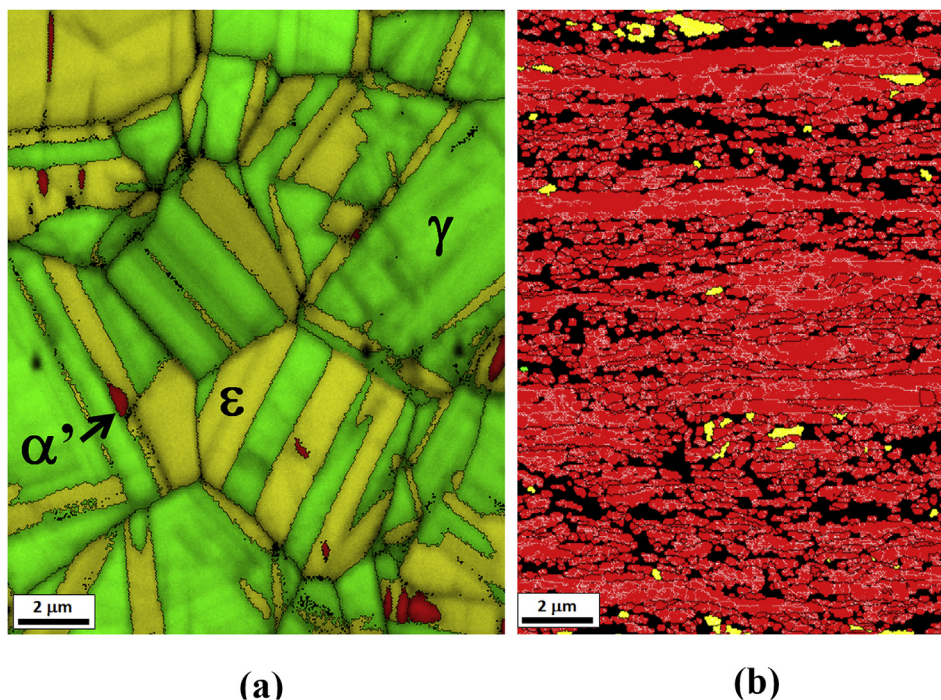
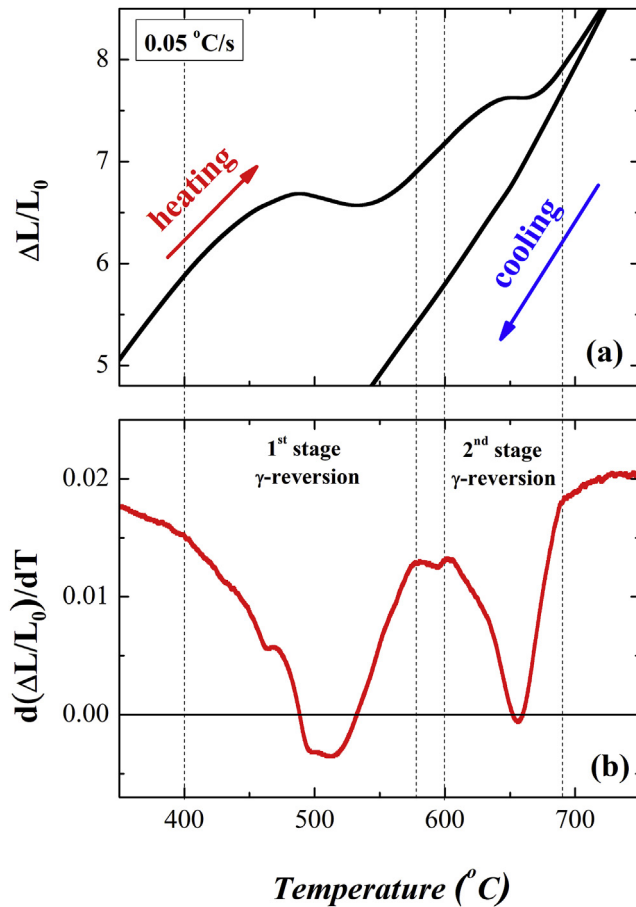


Fig. 1. EBSD phase maps: (a) as-received condition. (b) 80%-cold-rolled sample. In these maps, austenite,  $\varepsilon$ - and  $\alpha'$ -martensite are represented by green, yellow, and red, respectively. (For interpretation of the references to colour in this figure legend, the reader is referred to the Web version of this article.)



**Fig. 2.** Dilatometry measurements for the 80% cold-rolled steel. For this measurement the specimen was annealed from room temperature up to 800 °C with a heating rate of 0.05 °C/s. In this figure,  $L_0$  is the initial length of the specimen, taken parallel to the RD of the 80% cold-rolled plate. (a) Relative changes in length ( $\Delta L/L_0$ ) of the specimen. (b) Corresponding derivative curve  $d(\Delta L/L_0)/dT$  for the heating process.

until it sharply drops to values lower than 1 emu/g at 625 °C, evidencing that the Curie temperature of the remaining  $\alpha'$ -martensite has been reached. A careful inspection of Fig. 3 (a), however, reveals that a completely paramagnetic behavior is only reached for temperatures above  $\sim 750$  °C. By cooling the system in the presence of the external field, a low magnetic signal re-appears at  $\sim 750$  °C as shown in the inset of Fig. 3 (a). Such results allow us to infer that the analyzed sample presents a second Curie temperature at  $\sim 750$  °C, arising from a residual ferromagnetic phase.

Further metallographic inspection of the specimen subjected to this *in-situ* magnetic measurement reveals the absence of remaining  $\alpha'$ -martensite in the bulk, as demonstrated by Fig. 4 (a). Besides, we can clearly distinguish ferrite zones mixed with oxidized regions near the surface (Fig. 4b). This observation leads us to conclude that the formation of complex Fe-Mn-based oxides during the experiment allows the stabilization of Mn-depleted zones (ferrite) close to the surface, whose Curie temperature was found to be  $\sim 750$  °C [49,50].

### 3.3. Microstructural characterization at intermediate stages of the $\gamma$ -reversion

To obtain further microstructural information at intermediate stages of the  $\gamma$ -reversion, EBSD characterization was conducted on samples annealed up to 505 and 660 °C from dilatometry testing. As previously seen in Fig. 2 (a), such temperatures presented the

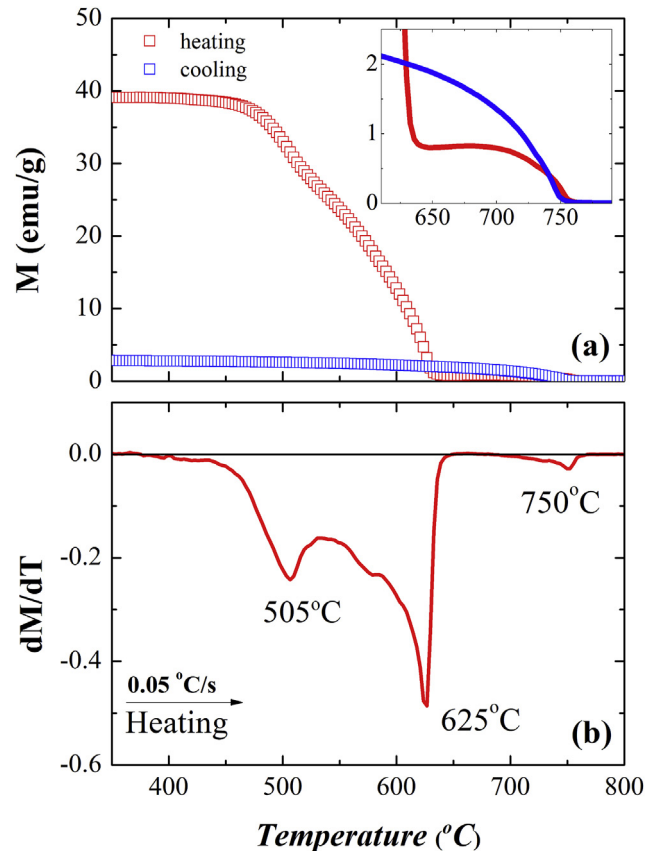


**Fig. 3.** (a) *In-situ* magnetic measurements (heating) conducted from room temperature up to 800 °C with a rate of 0.05 °C/s, in the presence of an external magnetic field of 90 Oe (red curve). The cooling process was performed using a rate of -0.05 °C/s with the same external magnetic field (blue curve). In this figure,  $M$  is the magnetization of the specimen at 90 Oe, given in emu/g. (b) Corresponding derivative curve ( $dM/dT$ ) for the heating process. (For interpretation of the references to colour in this figure legend, the reader is referred to the Web version of this article.)

maximum rate of contraction  $\frac{d(\frac{\Delta L}{L_0})}{dT}$  during annealing, i.e. the maximum rate of  $\gamma$ -formation. Fig. 5 (a) shows the phase map of the material annealed up to 505 °C, where we observe ultrafine reversed austenite ( $0.12 \pm 0.09 \mu\text{m}^2$ ) dispersed within a tempered  $\alpha'$ -matrix. Some austenite grains in this microstructure assume a near-equiaxial shape, while others are elongated. Fig. 5 (b) shows the phase map related to the sample continuously annealed up to 660 °C. In this case, we observe a predominant equiaxed microstructure, which is primarily austenitic, as expected. In turn, remaining  $\alpha'$ -martensite is dispersed in the microstructure displaying both equiaxed and elongated morphologies.

### 3.4. Diffusion-controlled transformations simulated using the DICTRA method

Diffusion simulations in the vicinity of the  $\gamma/\alpha'$  interface were performed by means of the DICTRA approach. For this purpose, a linear cell geometry with a planar interface between the phases is used as has been suggested in preceding studies [22]. In our case, the  $\alpha'$ -martensitic microstructure of the cold-rolled steel was represented by a cell of 1  $\mu\text{m}$  length. Fig. 6 (a) schematically shows the growth of a 0.3  $\mu\text{m}$  region corresponding to  $\gamma$  during the simulations. At this point, it is worth to mention that bcc  $\alpha'$ -martensite is usually taken as ferrite  $\alpha$  in thermodynamic calculations [22]. Although kinetic parameters may vary between ferrite and  $\alpha'$ -martensite due to lattice distortion and the enhanced dislocation

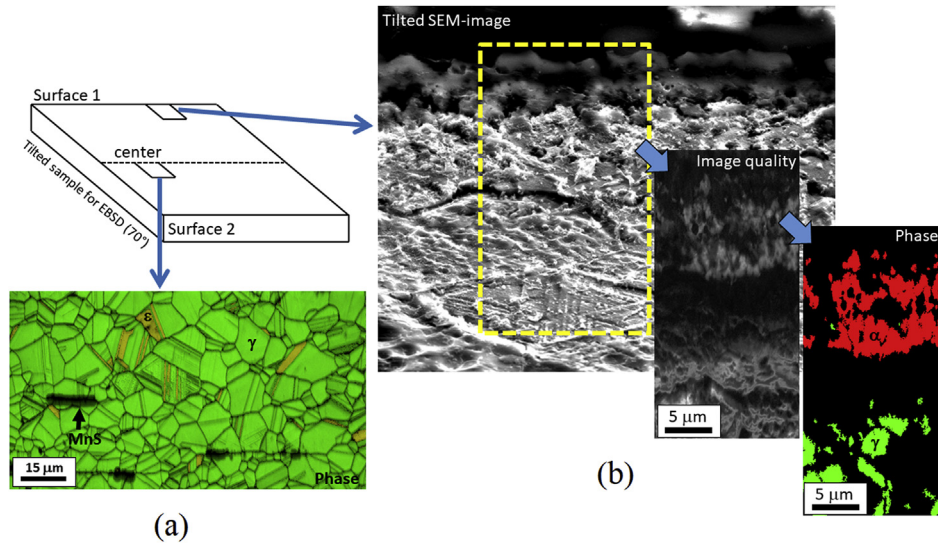


**Fig. 4.** Metallographic inspection of the 80% cold-rolled steel after being submitted to the *in-situ* magnetic measurements. EBSD maps were conducted in the central region of the sample (a), as well as near its surface (b).

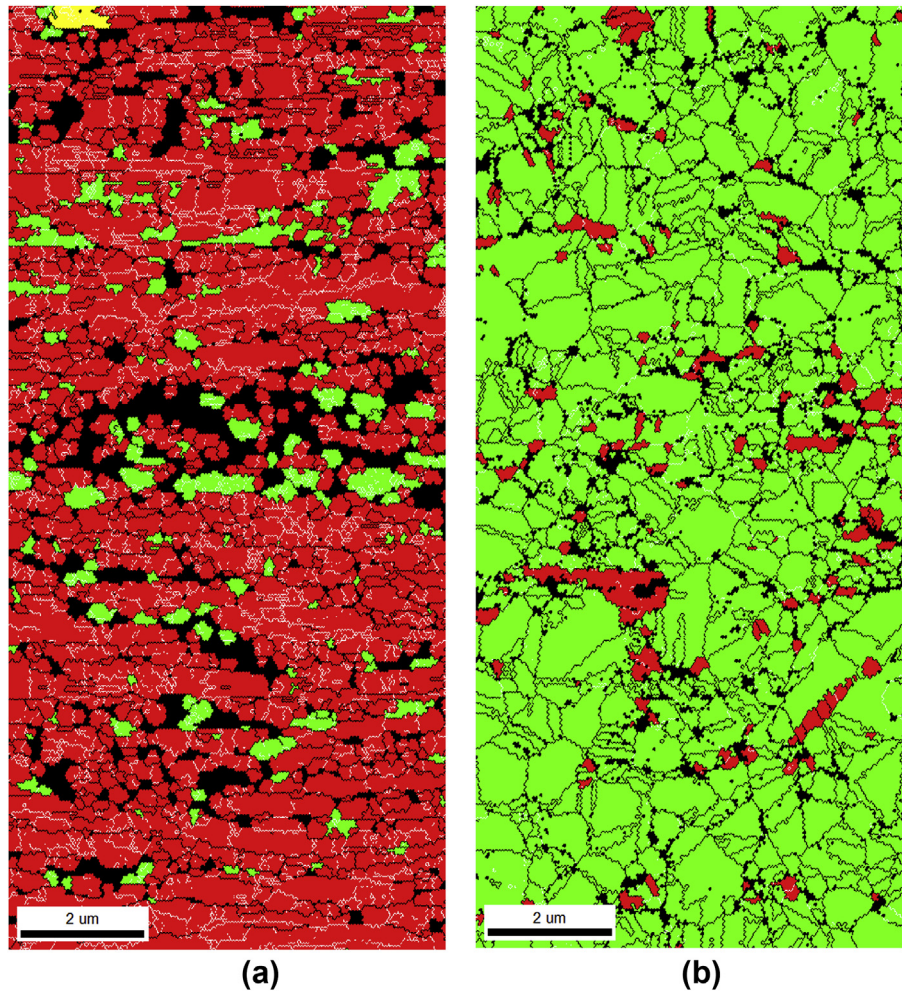


**Fig. 5.** (a) EBSD map of the 80% cold-rolled sample continuously annealed up to 505 °C. (b) EBSD map of the 80% cold-rolled steel continuously annealed up to 660 °C. In both figures, austenite and α'-martensite are represented by green and red, respectively. (For interpretation of the references to colour in this figure legend, the reader is referred to the Web version of this article.)

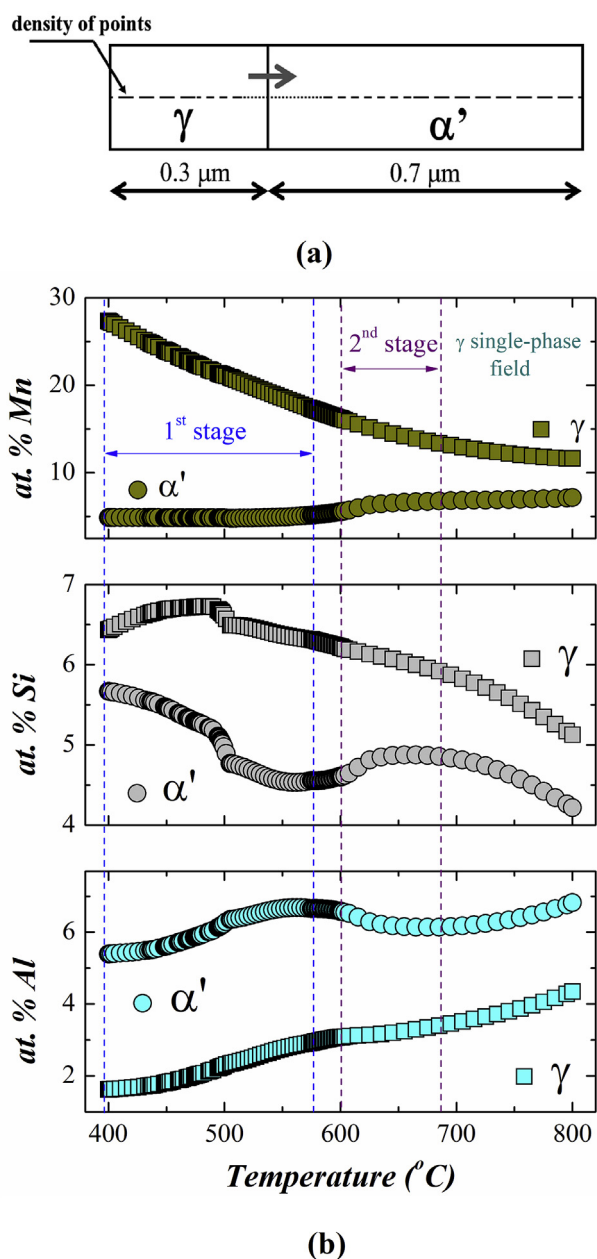


**Fig. 6.** (a). Schematic representation of the cell used for thermo-kinetic simulations (DICTRA). The cell (1  $\mu\text{m}$ ) shows the growth of a 0.3  $\mu\text{m}$  austenite as an example. The density of points becomes higher near the surface. (b) Changes in chemical composition across  $\gamma/\alpha'$  interface during continuous annealing with a heating rate of 0.05  $^{\circ}\text{C}/\text{s}$ , predicted by means of thermo-kinetics simulations with the aid of software DICTRA.

density, satisfactory results were obtained when using the ferrite parameters as will be shown below.

The cell was also discretized as a linear grid and set as a geometric series. The density of points becomes higher near the interface. The chemical composition adopted for  $\alpha'$  was the global chemical composition of the steel (Table 1). Because of the relatively low amounts of C and N in this steel only Fe, Mn, Al, and Si were considered in the kinetic DICTRA simulations. When C was included in the simulations, DICTRA did not succeed at finding the equilibrium point for austenite by considering that  $\text{M}_{23}\text{C}_6$  carbide is the stable phase at 400  $^{\circ}\text{C}$  rather than austenite. The possible effect

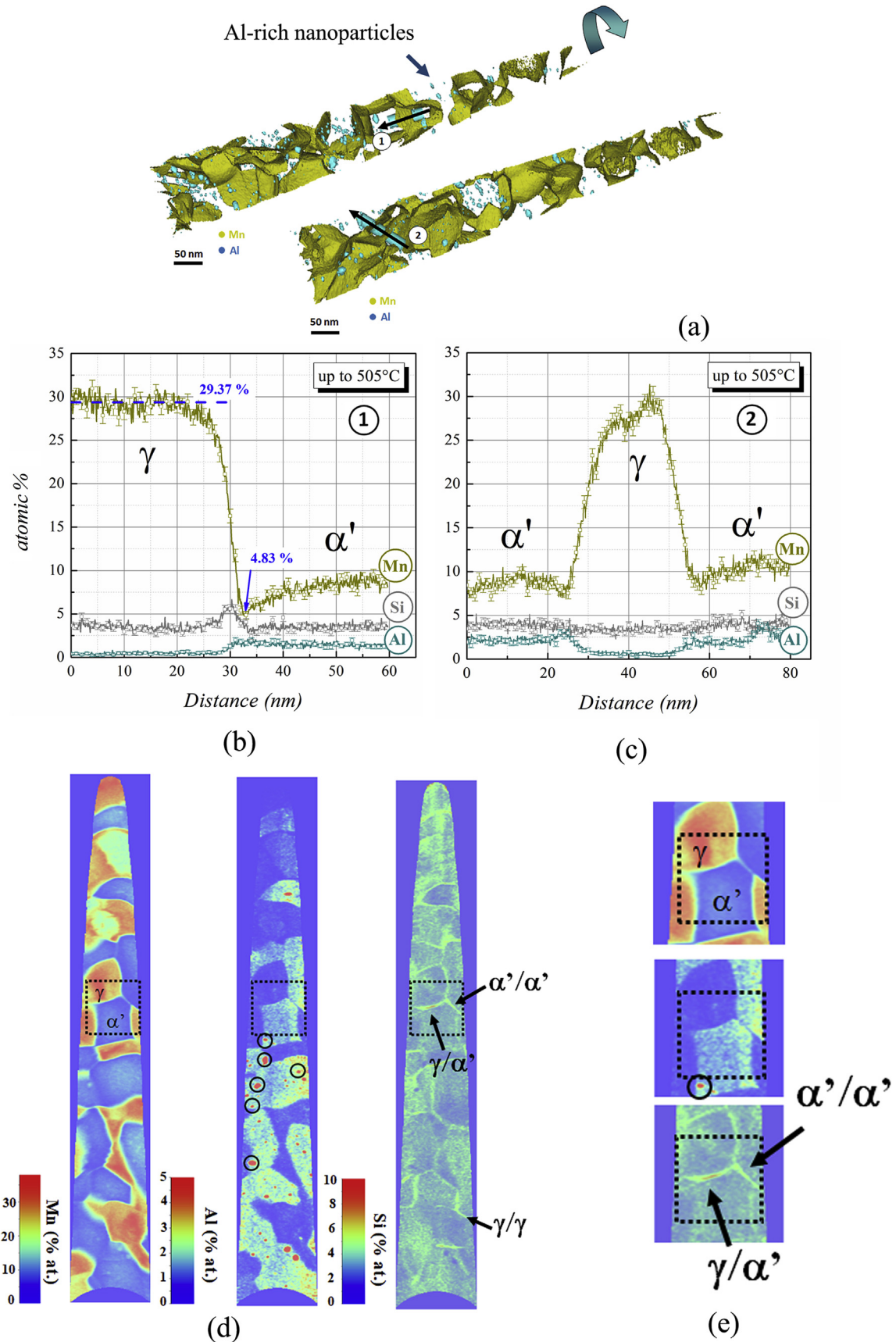
of C on the austenite reversion kinetics was discussed in Ref. [35]. It was shown that for a Fe7Mn0.5Si0.1C (wt.%) alloy annealed at 450  $^{\circ}\text{C}$ , Mn-enriched  $\gamma$ -nuclei can be poisoned by C and get converted into carbide nuclei, delaying the kinetics of  $\gamma$ -formation. For the present steel, we calculated the equilibrium amount of C remaining in the bcc  $\alpha'$ -martensite matrix after the possible formation of the  $\text{M}_{23}\text{C}_6$  with the aid of Thermo-Calc. Results showed that most of C is consumed by  $\text{M}_{23}\text{C}_6$  formation so that austenite nucleation and growth at 400  $^{\circ}\text{C}$  would occur in the near absence of C, allowing us to neglect C from DICTRA simulations. In Section 3.6, it will be demonstrated that there is a very good agreement between the kinetic simulations (without considering C) and the experimental results. These observations reveal that the thermo-kinetic simulations are sufficiently reliable, suggesting that the low amount of C in the present steel (0.19 at.%, which corresponds to 0.042 wt.%) plays a minor effect on austenite nucleation and growth. After setting the boundary conditions, the simulation was performed using a heating rate of 0.05  $^{\circ}\text{C}/\text{s}$  within the temperature range of 400–800  $^{\circ}\text{C}$ .

Fig. 6 (b) displays the DICTRA predicted changes in chemical composition across the  $\gamma/\alpha'$  interface over the course of the continuous annealing. The first important observation is the partitioning of Mn between  $\gamma$  and  $\alpha'$ . In fact, at the onset of the simulations (400  $^{\circ}\text{C}$ ), 27 at.% of Mn is observed on the  $\gamma$ -side of the interface whilst the  $\alpha'$ -side displays a drastically Mn-depleted zone with a composition of 4.9 at.%. As the annealing proceeds up to 600  $^{\circ}\text{C}$  (i.e. onset of the second stage of the  $\gamma$ -reversion), the composition of Mn in the austenite continuously decreases until reaching 16.20 at.%. The Mn-composition profile inside the  $\alpha'$ -martensite remains nearly unchanged up to 575  $^{\circ}\text{C}$ . From this temperature on, its composition slightly increases reaching a value of 5.53 at.% at 600  $^{\circ}\text{C}$ . Within the temperature range of 400–600  $^{\circ}\text{C}$ , an overall view of the chemical profiles shows that Si on the  $\gamma$ -side of the interface remains nearly unchanged with values of  $6.4 \pm 0.2$  at.%. On the  $\alpha'$ -martensite side, however, the Si content drops from 5.7 to 4.5 at.% at 600  $^{\circ}\text{C}$ . Regarding the Al compositions,  $\alpha'$ -martensite seems to be prone to retain a higher Al content during annealing. Both,  $\gamma$  and  $\alpha'$  adjacent to the interface display an increase in Al composition with increasing annealing temperature up to 600  $^{\circ}\text{C}$ . These results clearly support the observation that long-range diffusion is required within the temperature range of the first stage of the  $\gamma$ -reversion. As a consequence of the Mn depletion in the remaining martensite, its reversion is expected to be delayed to higher temperatures.

By continuing the simulations from 600  $^{\circ}\text{C}$  on, results suggest that the remaining  $\alpha'$ -martensite is stable not only along the second stage of the  $\gamma$ -reversion but also in the expected  $\gamma$  single-phase field. These results clearly deviate from the observations made by using dilatometry and *in-situ* magnetic measurements (Section 3.2). DICTRA simulations are based on diffusion-controlled reactions [40–42]. Therefore, the discrepancy presented here suggests that long-range partitioning does not entirely control the course of the second stage of the  $\gamma$ -reversion.

### 3.5. Atom probe tomography (APT) measurements

APT measurements were conducted for the sample annealed up to 505  $^{\circ}\text{C}$  to obtain detailed data on chemical gradients across the  $\gamma/\alpha'$  interfaces developed during the first stage of the  $\gamma$ -reversion. Fig. 7 (a) presents the three-dimensional reconstruction for the sample annealed up to 505  $^{\circ}\text{C}$ , for which two  $\gamma/\alpha'$  interfaces were investigated. In this figure, the blue arrow indicates the sense of rotation of the tomographic reconstruction to facilitate visualization of the second interface. Iso-composition surfaces for Mn (yellow) corresponding to threshold values of 20 at.% are also included



**Fig. 7.** Atom probe tomography results for the 80% cold-rolled sample continuously annealed up to 505 °C. **(a)** Three-dimensional reconstruction of the specimen. Yellow and blue spheres represent Mn and Al ions, respectively. The iso-composition surfaces for Mn were constructed by using a threshold value of 20 at.%. Blue clusters indicate Al-rich nanoparticles in  $\alpha'$ -martensite. **(b)** chemical profile obtained from the volume delimited by the cylinder "1" in (a). **(c)** chemical profile obtained from the volume delimited by cylinder "2" in (a). **(d)** two-dimensional composition maps obtained from the reconstructed specimens in (a). **(e)** Enlarged view of the black frames displayed in (d). (For interpretation of the references to colour in this figure legend, the reader is referred to the Web version of this article.)

in this figure. The precipitation of Al-rich nanoparticles is revealed in terms of iso-composition surfaces with a 5 at.% threshold in Fig. 7 (a). Further characterization of these precipitates is beyond the scope of the present work. Nevertheless, they seem to be formed within the remaining  $\alpha'$ -martensite indicating that precipitation aging in this phase can take place before or concurrently to  $\gamma$ -reversion.

The composition profiles calculated along the cylinders shown in Fig. 7 (a) are plotted in Fig. 7 (b) and (c). Mn compositions as high as 29.37 at.% can be found in the interior of  $\gamma$  whilst the remaining  $\alpha'$ -martensite contains only ~10 at.% of Mn. Furthermore, Mn-depletion is also noticeable near the interface on the  $\alpha'$ -side (4.83 at.%). Al seems to partition preferentially to  $\alpha'$ . At this point it is important to mention that these Al composition values may present a slight underestimation due to partial overlapping Fe and Al peaks in the mass spectrum [51]. In this case, one can also bear in mind the likely influence of instrumental parameters on non-preferential evaporation of certain ions [52]. The partitioning of Si at  $\gamma/\alpha'$  interfaces can be evaluated using the two-dimensional composition maps displayed in Fig. 7 (d). From this figure, both austenite and  $\alpha'$ -martensite can be clearly distinguished in terms of their respective compositions, particularly their Mn and Al content. The presence of Al-clusters is also evident within the  $\alpha'$ -martensite. Therefore, by using such differences in the Mn and Al content inside the grains, we can identify  $\gamma/\gamma$ ,  $\gamma/\alpha'$ , and  $\alpha'/\alpha'$  interfaces (see black frames in this figure). Additionally, Si accumulates to practically all of these interfaces and thus also helps revealing them in the APT data sets, as highlighted in Fig. 7 (e). At this point, one can bear in mind a minor influence of preferred evaporation of elements (i.e. instrumental artifacts) [52]. However, the most prominent cause for Si enrichment at the interfaces can be attributed to the differences of its kinetics within both  $\gamma$  and  $\alpha'$ , since solute partitioning takes place to keep the local equilibrium at the interfaces.

We conducted further APT analysis on a sample annealed at 600 °C for 5 min. An isothermal annealing treatment was performed and mapped by EBSD to ensure that representative regions were chosen for extracting specimens for APT probing, Fig. 8 (a). Also, this temperature lies in the vicinity of the Curie temperature (viz. 625 °C). In light of these observations, this short isothermal annealing at 600 °C should trigger the second stage of the  $\gamma$ -reversion. The corresponding reconstructed APT dataset is shown in Fig. 8 (b). Mn ions in this figure are represented by yellow spheres. The iso-composition surfaces for Mn, in turn, were constructed using a threshold value of 12 at.%. From the volume delimited by the cylinders in Fig. 8 (b), we collected chemical profiles, as displayed in the same figure. From these profiles, we still observe partitioning of Mn and Al across the  $\gamma/\alpha'$  interfaces. The compositions of Mn vary from ~18 to 24 at.% within the austenite, and ~6 at.% of Mn in the remaining  $\alpha'$ . Again, Al partitions to  $\alpha'$ , although no Al-rich particles were observed in this sample. Si segregation on the  $\gamma$ -side of the interface is also quite noticeable. For this condition, we also show as an example the C profile obtained from APT probing from the region highlighted by cylinder 1 (Fig. 8b). As expected, higher amounts of C are observed within  $\gamma$  compared to  $\alpha'$ -martensite. Accumulations of C at the left-hand side of the  $\gamma/\alpha'$  interface are also evident.

Fig. 8 (c) shows two-dimensional composition maps collected from the reconstructed specimen (Fig. 8 a). In this figure, it is possible to distinguish austenite and  $\alpha'$ -martensite grains due to the composition of their elements. Regarding Al and Mn profiles, we clearly see that heterogeneous distributions are present within  $\gamma$  and  $\alpha'$ . The presence of confined  $\gamma$ -zones with 24 at.% of Mn will be discussed below. In this figure, we also see local Si accumulation near the  $\gamma/\gamma$  and  $\gamma/\alpha'$  interfaces, whose composition ranges from 5 to 6 at.%. Similarly to Fig. 7 (d), solute partitioning is required to

keep the local equilibrium at the interfaces. Therefore, different Si kinetics between phases may explain its piling up. For this sample, however, no information regarding Si accumulation at  $\alpha'/\alpha'$  interface can be inferred since we did not succeed in acquiring such boundary type.

### 3.6. Comparison between DICTRA simulated and APT results

The changes in Mn composition across the moving  $\gamma/\alpha'$  interface simulated by DICTRA and displayed above in Fig. 6 (b) are reproduced in this section in the form of Mn-profiles for a continuous annealing process up to 505 °C (Fig. 9a) and 600 °C (Fig. 9b), respectively. For comparison, Figs. 9 (a) and (b) also display the Mn-profiles obtained from APT measurements as shown in Fig. 7 (b) and 8 (b) (cylinder 1), respectively. Fig. 9 clearly demonstrates that the partitioning behavior observed for Mn between  $\gamma$  and  $\alpha'$  is practically the same as the one predicted by the DICTRA simulations for the local equilibrium at the interface. As mentioned in Section 3.4, Thermo-Calc calculations showed that most of C in our steel is expected to be consumed during  $M_{23}C_6$  formation in the early beginning of the continuous annealing. Consequently, only a negligible amount of C would be available to participate of the  $\gamma$ -reversion. In light of these observations and the very good quantitative agreement revealed in Fig. 9 lead us to conclude that the low C content of the present steel (0.19 at.%, which corresponds to 0.042 wt.%) exerts only a minor effect on the austenite formation kinetics, differently from medium-Mn steels containing higher amounts of C (0.1 wt.%) [35]."

## 4. Discussion

### 4.1. Thermodynamic simulations and dilatometry results

Fig. 10 shows an isopleth of the Fe-Mn-Al-Si-C system, calculated using Thermo-Calc. Differently from the kinetic simulations (section 3.4), here C was also considered for the thermodynamic simulations. In Fig. 10, the chemical composition of the present steel is highlighted, as well as the start ( $A_s$ ) and finish ( $A_f$ ) temperatures for both  $\gamma$ -reversion stages. By using the lever rule and taking into account the dilatometry values of  $\frac{\Delta L}{L_0}$  from Fig. 2 (a), the volume fractions of austenite during continuous annealing were also determined [53] and values are reported in Fig. 10. In this figure, the experimental value for  $A_s^{1st-stage}$  lies approximately in the beginning of the intercritical field ( $\alpha + \gamma$ ). However, at  $A_f^{1st-stage} = 575$  °C, 42% of the microstructure is still composed of remaining  $\alpha'$ -martensite. In other words, the  $\alpha' \rightarrow \gamma$  transformation is not complete when the  $\gamma$  single-phase field is expected to initiate, viz. at 585 °C. As previously observed by means of APT and DICTRA simulations, such differences arise from the strong chemical partitioning between  $\gamma$  and  $\alpha'$ . The thermodynamic equilibrium used as a basis for constructing Fig. 10 provides only long-term (infinite) partitioning ranges and phase regions. However, the growth of austenite is controlled by local equilibrium (LE) at the interface [19,22]. For instance, at  $A_f^{1st-stage}$ , the  $\gamma/\alpha'$  interface grows towards  $\alpha'$  under a local equilibrium given by 17.3 and 5.1 at.% of Mn at  $\gamma$  and  $\alpha'$  sides, respectively (see Fig. 6). As a first consequence, the chemical composition of reversed austenite differs considerably from the global chemical composition of the steel (Table 1). Due to such changes, new equilibrium conditions are established and the remaining depleted-solute  $\alpha'$  transforms into  $\gamma$  at higher temperatures. In addition, the second peak associated with the reversion occurs just after the loss of ferromagnetism of the remaining  $\alpha'$  (625 °C), i.e. the remaining  $\alpha'$  transforms back to austenite in a state of paramagnetism.

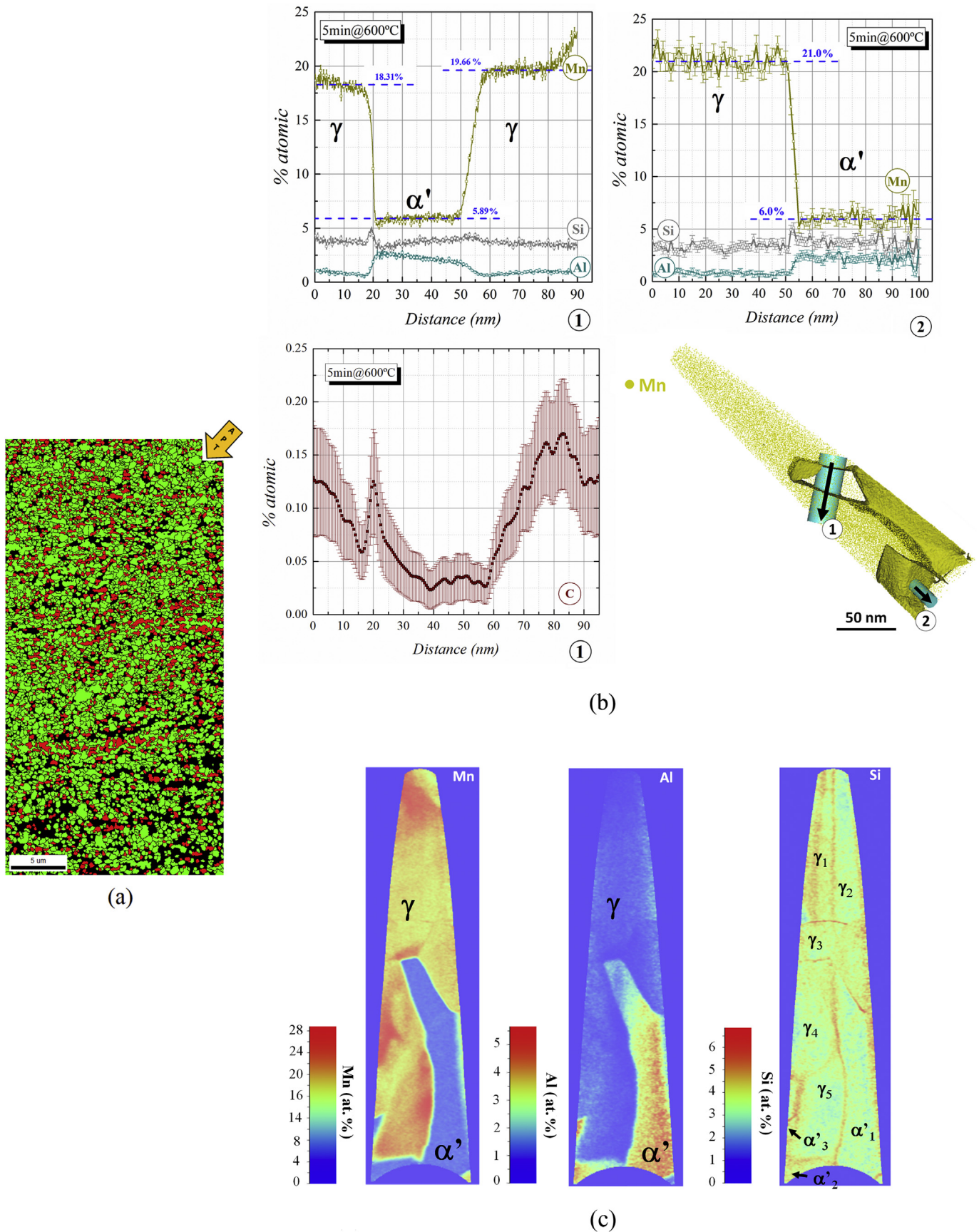


**Fig. 8.** (a) EBSD map of the 80% cold-rolled steel isothermally annealed at 600 °C for 5 min. Green and red regions represent austenite and remaining α', respectively. (b) Corresponding three-dimensional reconstructed APT specimen. Yellow spheres represent Mn ions. Iso-composition surfaces were constructed with a threshold value of 12 at.%. The chemical profiles displayed in this figure were taken from the cylinders labeled as "1" and "2" within the reconstructed specimen. (c) Two-dimensional composition maps taken from (b). (For interpretation of the references to colour in this figure legend, the reader is referred to the Web version of this article.)

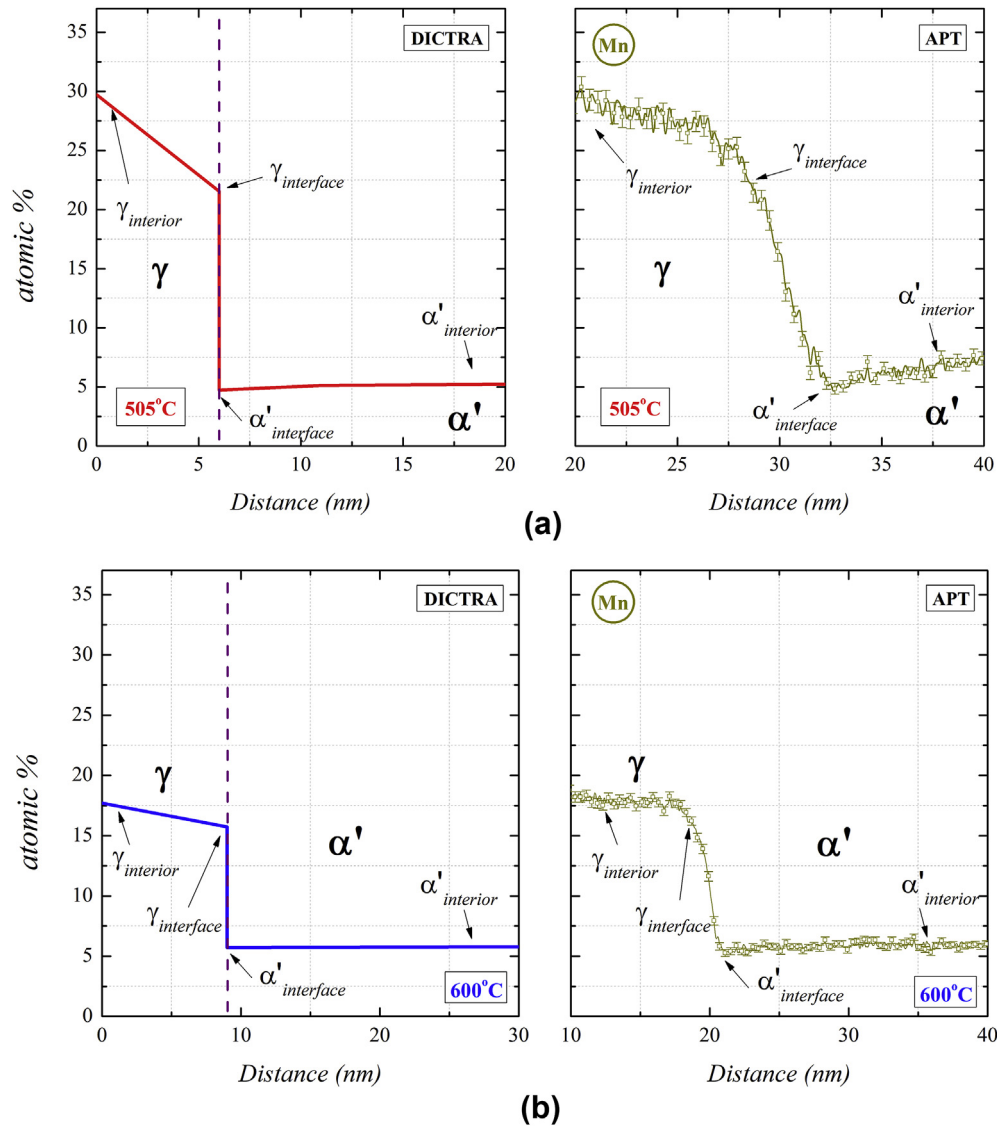


**Fig. 9.** Comparison between the Mn profiles obtained via APT with those obtained via DICTRA simulations (where no C content was included in the calculation) for (a) the continuous annealing up to 505 °C and (b) at 600 °C.

#### 4.2. $\gamma$ -reversion mechanisms

After nucleation, austenite grows essentially by either a diffusion- or an interface-controlled mechanism. The former involves long-range diffusion of elements, while for the latter, diffusion takes place only in a short-range, i.e. near the moving  $\gamma/\alpha'$  interface. In this case, both parent and product phases assume the same chemical composition, i.e. the transformation proceeds locally partitionless [54]. For the steel studied, Fig. 11 shows the driving force for austenite formation driven by long-range (partitioning) and short-range (partitionless) diffusion. In this context, the driving force demonstrates how far the system is driven locally from the global equilibrium suggested by the phase diagram. The driving force magnitude for the  $\alpha' \rightarrow \gamma$  reaction controlled by the long-range partitioning regime was evaluated according to the approach implemented in Thermo-Calc for driving force calculations. For the present case, the partitioning driving force is approximated as the local difference in free energy between the matrix ( $\alpha'$ ) and the equilibrium point of a  $\alpha'/\gamma$  mixture. It is worth mentioning that the additional free energy contribution due to the

capillarity of the nucleus (interfacial energy) is not considered in such procedure. The partitionless driving force, in turn, is given by the difference in free energy of the parent and product phases.

In Fig. 11,  $T_0$  is the temperature where the free energies of  $\gamma$  and  $\alpha'$ -martensite are identical (without taking into account the additional free energy contribution due to the capillarity of the nucleus). For temperatures below  $T_0 = 350$  °C, the partitionless driving force is negative and the  $\gamma$ -reversion can only be driven by the partitioning mechanism. In this work, we notice that the temperature of the onset of the  $\gamma$ -reversion is higher than  $T_0$ ; i.e., in the temperature range where both mechanisms could be expected. However, the pronounced elemental partitioning observed by APT and DICTRA simulations between the adjacent phases (Fig. 6) suggests that the  $\gamma$ -reversion is mainly driven by the partitioning mechanism at its onset. By increasing the temperature to a value above  $T_0$ , the behavior of both, the partitioning and the partitionless curves, displays opposite trends. However, within the range of 350–660 °C, the driving force for a partitioning reversion is always higher than the corresponding value obtained when assuming a partitionless transformation mechanism. The progress of the  $\alpha' \rightarrow$

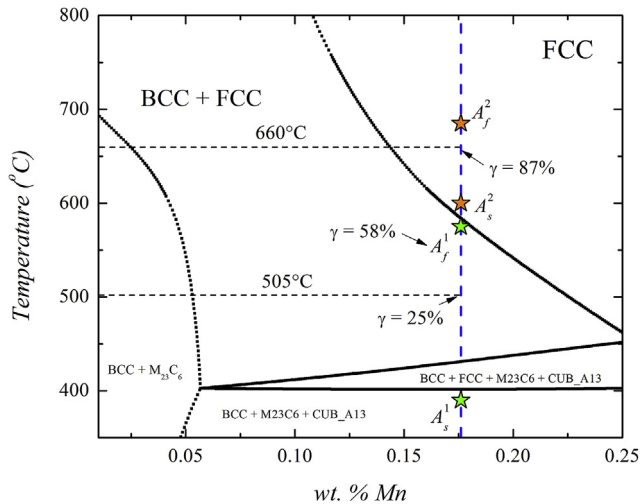


**Fig. 10.** Isoleth of the Fe-Mn-Al-Si-C system. The global chemical composition of the present steel is highlighted by the blue-dashed vertical line. The start ( $A_s^1$ ) and finish ( $A_f^1$ ) temperatures for the first stage of  $\gamma$ -reversion are indicated by green stars; Analogously,  $A_s^2$  and  $A_f^2$  for the second stage of  $\gamma$ -reversion are represented by orange stars. The volume fraction of austenite for representative temperatures is represented as well. (For interpretation of the references to colour in this figure legend, the reader is referred to the Web version of this article.)

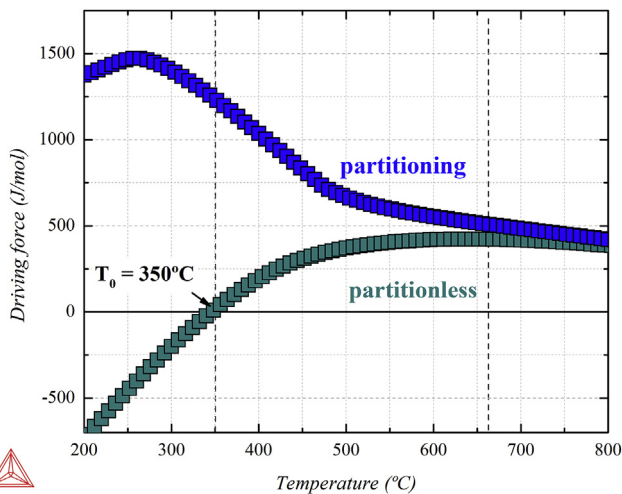


**Fig. 11.** Driving force for austenite formation driven by partitioning and partitionless mechanisms.  $T_0$  denotes the temperature where the free Gibbs energy of both austenite and  $\alpha'$ -martensite is the same.

$\gamma$  reaction is hence mainly achieved by means of long-range diffusion during the first stage of austenite reversion, which is supported by the drastic chemical composition changes observed between the growing austenite and the remaining  $\alpha'$ -martensite as revealed by APT data.

Yet in Fig. 11, the driving forces for both mechanisms seem to be the same for temperatures above 660 °C. From the dilatometry measurements (Fig. 2a), the second stage of  $\gamma$ -reversion extends to a narrower range of temperature (85 °C) when compared to the first one. Furthermore, the derivatives of these curves (Fig. 2 b) show that the magnitude of contraction associated to this stage is smaller, as reported in other studies [30]. According to Ref. [30], such observations indicate a partitionless mechanism ruling the  $\gamma$ -reversion. Diffusion-based DICTRA simulations performed within the temperature range of 600–800 °C (Fig. 6) predicted the stabilization of the remaining  $\alpha'$ -martensite until the expected  $\gamma$  single-

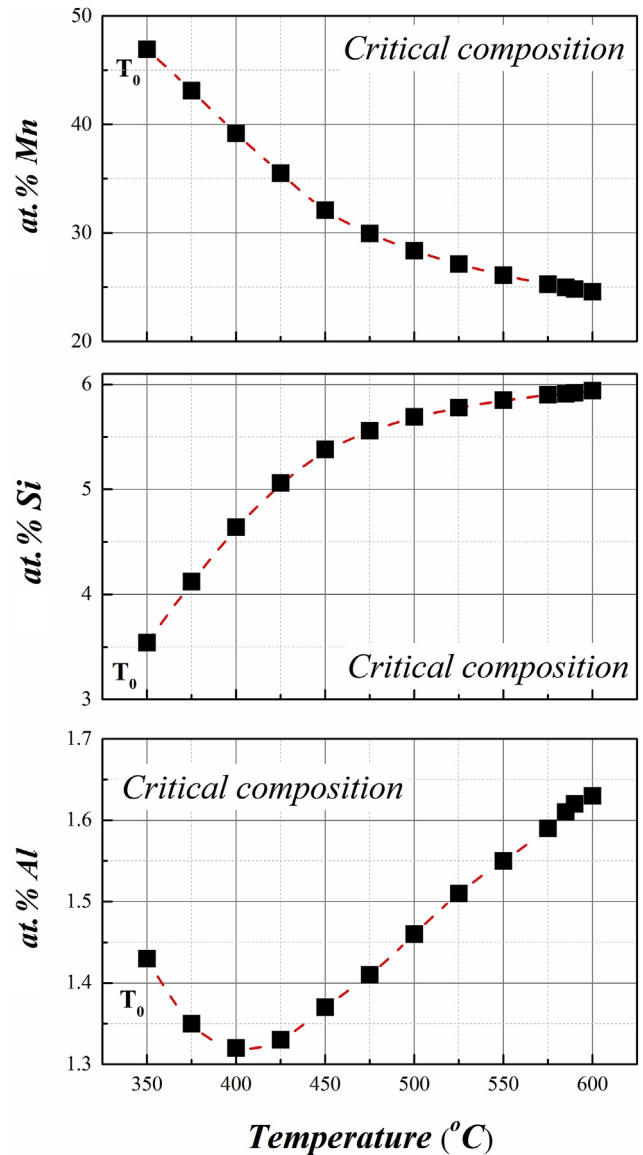


**Fig. 12.** Critical composition of the  $\gamma$ -nucleus for several temperatures, calculated according to the parallel tangent construction in free energy curves as reported in Ref. [55].

phase field. Such results clearly deviate from the experimental observations made by dilatometry. Therefore, it is plausible to infer that the partitioning mechanism is not the major responsible mechanism for transforming  $\alpha'$ -martensite from 660 °C on in this steel.

#### 4.3. $\gamma$ -nucleation and growth

In this section, we discuss the  $\gamma$ -nucleation and growth with the aid of thermo-kinetic simulations combined with experimental observations made via APT. Owing to the Gibbs-Thomson effect, the chemical composition of  $\gamma$ -nuclei may differ from the equilibrium composition of the  $\alpha'/\gamma$  mixture given by the lever-rule [54,56]. Bearing such effect in mind, we calculated the composition of a critical nucleus adopting the “parallel tangent construction” in diagrams  $G_p$  vs  $x_i$ , where  $G_p$  is the free energy of a phase “p”; and  $x_i$  the molar fraction of an element “i” [55]. Fig. 12 shows the composition of the critical  $\gamma$ -nucleus within the temperature range of

350–600 °C for the present steel.

At the onset of the first (~400 °C) and second (600 °C) stages of the  $\gamma$ -reversion, the critical  $\gamma$ -nuclei display compositions of Mn considerably higher than the global chemical composition of the steel (viz. Mn = 16.9 at.%; Al = 3.4 at.%; Si = 6.1 at.%). Contrastingly, relative lower amounts of Si and Al are observed in the critical  $\gamma$ -nuclei. Results from Fig. 12 demonstrate once again the importance of long-range diffusion and elemental partitioning for providing the local chemical concentrations and thus driving forces required for a successful  $\gamma$ -nucleation event. In a recent work, Kwiatkowski da Silva et al. [57] showed that such chemical fluctuations in Fe-Mn alloys are caused by the segregation of Mn to the grain boundaries followed by the formation of spinodal-like fluctuations. These local compositional variations can be regarded as intermediate precursor states preceding the actual reversion. In other words, local spinodal Mn enrichment lowers the remaining barriers for nucleation. In light of these observations, we assume that  $\gamma$ -nucleation at a given temperature may occur predominantly at Mn enriched regions, whose composition reaches those values displayed in Fig. 12.

#### 4.3.1. $\gamma$ -nucleation and growth at 500 °C

To better understand the growth of  $\gamma$ -nuclei, we conducted further thermo-kinetic simulations reproducing isothermal annealings at 500 °C and 600 °C. Fig. 13 shows the composition

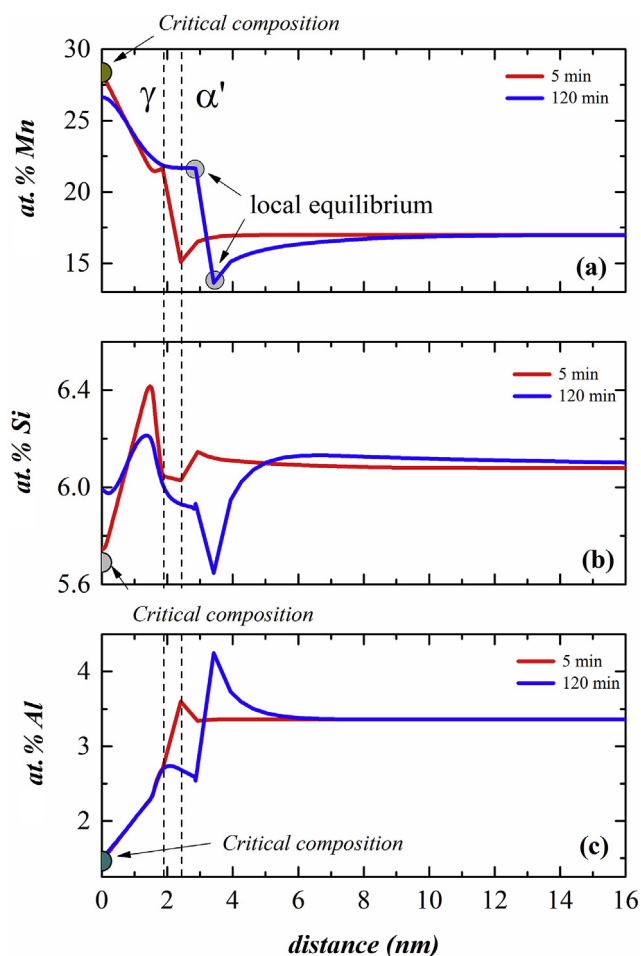


**Fig. 13.** Evolution of chemical profiles across  $\gamma/\alpha'$  interface during austenite growth at 500 °C. Results obtained by means of thermo-kinetics simulation using DICTRA. The corresponding critical composition of each element is also highlighted. Chemical profiles shown in terms of (a) Mn; (b) Si; (c) Al. The dotted vertical lines represent the position of the  $\gamma/\alpha'$  interface for a time of 5 min.

profiles across  $\gamma/\alpha'$  interfaces after 5 and 120 min at 500 °C. In this figure, the critical composition of the nucleus is indicated by arrows. After 5 min, the Mn content of the former nucleus is nearly equal to the critical one (Fig. 13 a). Concerning Si in Fig. 13 (b), we notice its pronounced piling up tendency (6.4 at.%) on the  $\gamma$ -side of the interface, after 5 min. DICTRA approach makes no consideration related to effects of solute drag on the mobility of the interface [41]. Therefore, the different Si kinetics within  $\gamma$  and  $\alpha'$  may explain its pile up near the moving  $\gamma/\alpha'$  interfaces.

After 120 min, the composition of the nucleus slightly depletes in Mn (Fig. 13 a). In fact, such reduction is expected to occur until reaching the local equilibrium that rules the interface motion. However, the simulations displayed in Fig. 13 show that homogenization of the growing austenite proceeds slow, due to the fact that the diffusion rates of Mn in austenite are low [22]. In an opposite trend, the Si content in the former nucleus enriches to values similar to the local equilibrium of the interface (120 min). After 120 min, lower levels of Si accumulation in  $\gamma$  remain near the moving interface (Fig. 13 b). This observation suggests that the former Si-enriched interfacial zone is gradually redistributed within  $\gamma$  with progressing annealing time. On the  $\alpha'$ -side, the presence of a Si-depleted zone near the interface indicates a mass flux of Si towards  $\gamma$ . These simulations show the importance of local Si enrichment on the homogenization of  $\gamma$ . These results also demonstrate that  $\gamma$ -growth is followed by a significant consumption of Si from the  $\alpha'$ -martensite. Finally, Fig. 13 (c) indicates that the local Al accumulation on the  $\alpha'$ -side moves jointly with the interface. An overall view of Fig. 13 shows that  $\gamma$ -homogenization is preceded by local accumulation of Si and Al.

The Si piling up trend is clearly supported by means of the two-dimensional composition maps (APT) displayed in Fig. 7, where Si-enriched interfaces were observed with similar compositions as those observed in Fig. 13.

#### 4.3.2. $\gamma$ -nucleation and growth at 600 °C

Experimental observations of nucleation events are challenging. Nevertheless, Fig. 8 (b) throws light onto nuclei formed at 600 °C. As an example, regions containing approximately 24 at.% Mn appear in the profile calculated from cylinder “1” in Fig. 8 (b), at a position of about 90 nm in the “x” axis. Notice that this value is similar with the critical composition at 600 °C (5.9 at.% Si, 24.6 at.% Mn, and 1.6 at.% Al), which strongly suggests the presence of a former  $\gamma$ -nucleus.

Using both chemical composition and phase size obtained experimentally in Fig. 8, additional simulations were performed and the results are shown in Fig. 14. The calculated critical compositions are also highlighted. Fig. 14 (a) shows that the Mn content of the nucleus gradually decreases to 18 at.% for 120 min simulation time at 600 °C. As mentioned in Section 4.3.1, this decrease is expected until compositional homogenization of the austenite is reached. Regarding Si, Fig. 14 (b) shows that accumulation near the interface is present in the beginning of the simulation. However, as the annealing proceeds, the Si profile broadens and a relatively homogenous composition is found in austenite. Consequently, the former nucleus slightly enriches in Si. Finally, no significant changes are observed for the Al profile in austenite. For 120 min, the Al profile is homogenous in the  $\alpha'$ -martensite and the former local accumulation is not observed anymore. This result also shows that compositional  $\gamma$ -homogenization is controlled by the redistribution of piled-up solutes, as discussed in Section 4.3.1.

#### 4.4. Influence of elemental partitioning on the Curie temperature

With the aid of Thermo-Calc, we calculated the  $T_{\text{Curie}}$  of the present steel taking into account several chemical compositions for

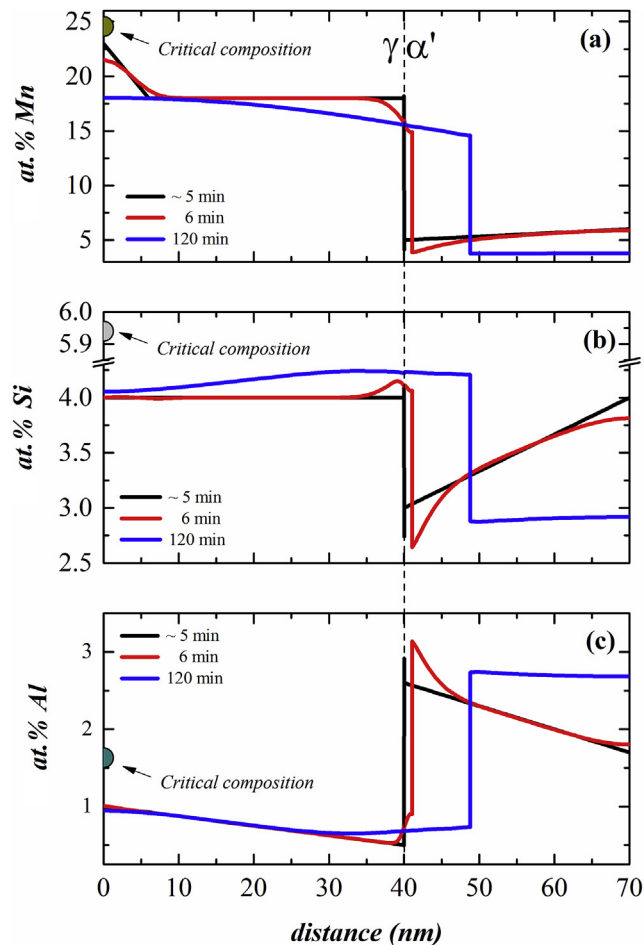


**Fig. 14.** Evolution of chemical profiles across  $\gamma/\alpha'$  interface during austenite growth at 600 °C. Results obtained by means of thermo-kinetics simulation using DICTRA. The starting chemical composition were taken from the experimental APT results displayed in Fig. 8. The corresponding critical composition of each element is also highlighted. Chemical profiles shown in terms of (a) Mn; (b) Si; (c) Al. The dotted vertical line represents the position of the  $\gamma/\alpha'$  interface for a time of ~5 min.

**Table 2**

Curie temperatures of  $\alpha'$ -martensite predicted for different chemical compositions, taken from APT measurements and predicted with the aid of DICTRA, as well as the experimentally observed Curie temperature.

Condition	at.% Mn	at.% Si	at.% Al	$T_{\text{Curie}}$ (°C)
$\epsilon = 1.56$ cold-rolled	16.9	6.1	3.4	445
up to 600 °C (DICTRA)	5.54	4.61	6.59	632
isothermal at 600 °C (APT, cylinder 1)	5.89	3.64	2.30	653
isothermal at 600 °C (APT, cylinder 2)	6.02	3.67	2.20	651
<i>in-situ</i> magnetic measurements	–	–	–	625

the  $\alpha'$ -martensite reported in this work. Table 2 summarizes the results from our simulations in comparison to the experimental  $T_{\text{Curie}}$  (625 °C). This table shows that if no long-range diffusion had occurred during annealing, the chemical composition of the  $\alpha'$ -martensite would have been the same as the global chemical composition. Therefore, a  $T_{\text{Curie}}$  of 445 °C would be expected. On the other hand, the chemical compositions of the  $\alpha'$ -martensite experimentally determined via APT and simulated using DICTRA are in good agreement. Smaller Al contents in APT specimens are likely caused by instrumental errors, as already discussed. In spite of this, all values of  $T_{\text{Curie}}$  corresponding to these compositions are in very good agreement with the experimental value of 625 °C.

They also agree with a recent study on the influence of partitioning on the Curie temperature reported by Dastur et al. [36] for a steel containing 18 wt.% Mn, 2 wt.% Al, 2 wt.% Si, and 0.04 wt.% C. These results show that elemental partitioning which occurs during austenite nucleation and growth strongly influences the ferromagnetic behavior of  $\alpha'$ -martensite.

## 5. Summary and conclusions

We studied austenite reversion in a cold-rolled 17.6 wt.% Mn steel during slow continuous annealing by means of dilatometry and *in-situ* magnetic measurements. In light of the results reported in this work the following conclusions are drawn:

During slow continuous annealing, austenite reversion is not yet complete when the equilibrium  $\gamma$  single-phase field as predicted by Thermo-Calc is reached. According to thermo-kinetic simulations, strong elemental partitioning is required for austenite nucleation and growth, as was clearly confirmed by APT. The APT results showed that Mn-enriched regions corresponded to reversed- $\gamma$  while Mn-depleted zones were the remaining  $\alpha'$ -martensite. Due to its lower Mn content, the remaining  $\alpha'$  experienced the  $\alpha' \rightarrow \gamma$  reaction at higher temperatures. Therefore, austenite reversion during continuous heating was observed to be split into two stages, with maximum transformations rates at 505 and 660 °C. The second peak, i.e. the second distinct step of the austenite reversion (660 °C) occurred for a paramagnetic  $\alpha'$ -martensite, whose Curie temperature was 625 °C.

Under isothermal conditions at 500 and 600 °C, thermo-kinetic simulations demonstrated that the compositional homogenization of growing austenite is determined by the redistribution of the piled-up solutes, especially of Si. Such simulations were also confirmed by means of APT, which clearly demonstrated the strong tendency of local Si accumulation to interfaces, occurred to keep the local equilibrium.

Finally, we calculated the Curie temperature of the alloy taking into account the chemical composition of the remaining  $\alpha'$  determined via simulations and APT. It turned out that the obtained values hold excellent agreement with the experimental value of 625 °C, determined by *in-situ* magnetic measurements. Therefore, we also conclude that elemental partitioning influences not only austenite nucleation and growth but also the ferromagnetic behavior of the  $\alpha'$ -martensite.

## Acknowledgments

This work is partially supported by FAPESP – Sao Paulo Research Foundation (Brazil, Grant number 2017/04444-1). Authors are grateful to Prof. Dr. D. B. dos Santos (DEMET-UFMG) for kindly supplying the steel used in this investigation and to R. Cohen and Dr. L. C. M. Nagamine (IF-USP) for the *in-situ* magnetic measurements. The authors are also grateful to U. Tezins and A. Sturm for their technical support of the atom probe tomography and focused ion beam facilities at the Max-Planck-Institut für Eisenforschung. IRSF thanks to FAPESP (Grants number: 2015/26409-8 and 2017/17170-7) for his scholarships. AKS is grateful to CNPq (Brazilian National Research Council) for his scholarship (Grant number: 203077/2014-8). HRZS and MJRS are CNPq Fellows under Grants 302.136/2017-7 and 303.826/2015-0, respectively.

## References

- [1] G. Frommeyer, U. Brück, Microstructures and mechanical properties of high-strength Fe-Mn-Al-C light-weight TRIPLEX steels, *Steel Res. Int.* 77 (2006) 627–633.
- [2] B.C. De Cooman, K.G. Chin, J. Kim, High Mn TWIP steels for automotive applications, in: Marcello Chiaberge (Ed.), *New Trends and Developments in*

- Automotive System Engineering, 2011. ISBN: 978-953-307-517-4.
- [3] H. Kim, D.-W. Suh, N.J. Kim, Fe-Al-Mn-C lightweight structural alloy: a review on the microstructures and mechanical properties, *Sci. Technol. Adv. Mater.* 14 (2013) 014205.
  - [4] D. Raabe, H. Springer, I. Gutierrez-Urrutia, F. Roters, M. Bausch, J.B. Seol, M. Koyama, P.P. Choi, K. Tsuzaki, Alloy design, combinatorial synthesis, and microstructure-property relations for low-density Fe-Mn-Al-C austenitic steels, *JOM (J. Occup. Med.)* 66 (2014) 1845–1856.
  - [5] J. Zhang, D. Raabe, C.C. Tasan, Designing duplex, ultrafine-grained Fe-Mn-Al-C steels by tuning phase transformation and recrystallization kinetics, *Acta Mater.* 141 (2017) 374–387.
  - [6] O. Grässel, L. Krüger, G. Frommeyer, L.W. Meyer, High strength Fe-Mn-(Al,Si) TRIP/TWIP steels development – properties – application, *Int. J. Plasticity* 16 (2000) 1391–1409.
  - [7] S.L. Wong, M. Madivala, U. Prah, F. Roters, D. Raabe, A crystal plasticity model for twinning- and transformation-induced plasticity, *Acta Mater.* 118 (2016) 40–151.
  - [8] A. Saeed-Akbari, J. Imlau, U. Prah, W. Bleck, Derivation and variation in composition-dependent stacking fault energy maps based on subregular solution model in high-manganese steels, *Metall. Mater. Trans. A* 40 (13) (2009) 3076–3090.
  - [9] D.T. Pierce, J.A. Jiménez, J. Bentley, D. Raabe, C. Oskay, J.E. Wittig, The influence of manganese content on the stacking fault and austenite/ $\epsilon$ -martensite interfacial energies in Fe–Mn–(Al–Si) steels investigated by experiment and theory, *Acta Mater.* 68 (2014) 238–253.
  - [10] L. Remy, A. Pineau, Twinning and strain-induced F.C.C.  $\rightarrow$  H.C.P. transformation in the Fe-Mn-Cr-C system, *Mater. Sci. Eng.* 28 (1) (1977) 99–107.
  - [11] A. Sato, K. Soma, T. Mori, Hardening due to pre-existing  $\epsilon$ -Martensite in an Fe-30Mn-1Si alloy single crystal, *Acta Metall.* 30 (10) (1982) 1901–1907.
  - [12] S. Allain, J.-P. Chateau, O. Bouaziz, S. Migot, N. Guelton, Correlations between the calculated stacking fault energy and the plasticity mechanisms in Fe-Mn-C alloys, *Mater. Sci. Eng.*, A 387–389 (2004) 158–162.
  - [13] S.T. Pisarik, D.C. Van Aken, Thermodynamic driving force of the  $\gamma \rightarrow \epsilon$  transformation and resulting Ms temperature in high-Mn steels, *Metall. Mater. Trans. A* 47 (2016) 1009–1018.
  - [14] G.B. Olson, M. Cohen, Kinetics of strain-induced martensitic nucleation, *Metall. Trans. A* 6 (4) (1975) 791–795.
  - [15] J.B. Leblond, G. Mottet, J.C. Devaux, A theoretical and numerical approach to the plastic behaviour of steels during phase transformations -I. Derivation of general relation, *J. Mech. Phys. Solid.* 34 (4) (1986) 395–409.
  - [16] J.B. Leblond, G. Mottet, J.C. Devaux, A theoretical and numerical approach to the plastic behaviour of steels during phase transformations – II. Study of classical plasticity for ideal-plastic phases, *J. Mech. Phys. Solid.* 34 (4) (1986) 411–432.
  - [17] R.G. Stringfellow, D.M. Parks, G.B. Olson, A constitutive model for transformation plasticity accompanying strain-induced martensitic transformations in metastable austenitic steels, *Acta Metal. Mater.* 40 (7) (1992) 1703–1716.
  - [18] L. Bracke, L. Kestens, J. Penning, Transformation mechanism of  $\alpha'$ -martensite in an austenitic Fe–Mn–C–N alloy, *Scripta Mater.* 57 (2007) 385–388.
  - [19] D. Raabe, S. Sandlöbes, J. Millán, D. Ponge, H. Assadi, M. Herbig, P.-P. Choi, Segregation engineering enables nanoscale martensite to austenite phase transformation at grain boundaries: a pathway to ductile martensite, *Acta Mater.* 61 (2013) 6132–6152.
  - [20] D.P. Escobar, S.S.F. Dafé, D.B. Santos, Martensite reversion and texture formation in 17Mn-0.06C TRIP/TWIP steel after hot cold rolling and annealing, *J. Mater. Res. Technol.* 4 (2) (2015) 162–170.
  - [21] P. Dastur, A. Zarei-Hanzaki, M.H. Pishbin, M. Moallemi, H.R. Abedi, Transformation and twinning induced plasticity in an advanced high Mn austenitic steel processed by martensite reversion treatment, *Mater. Sci. Eng.*, A 696 (2017) 511–519.
  - [22] O. Dmitireva, D. Ponge, G. Inden, J. Millán, P. Choi, J. Sietsma, D. Raabe, Chemical gradients across phase boundaries between martensite and austenite in steel studied by atom probe tomography and simulation, *Acta Mater.* 59 (2011) 364–374.
  - [23] N. Nakada, Y. Arakawa, K.S. Park, T. Tsuchiyama, S. Takaki, Dual phase structure formed by partial reversion of cold-deformed martensite, *Mater. Sci. Eng.*, A 553 (2012) 128–133.
  - [24] N. Nakada, T. Tsuchiyama, S. Takaki, D. Ponge, D. Raabe, Transition from diffusive to displacive austenite reversion in low-alloy steel, *ISIJ Int.* 53 (12) (2013) 2275–2277.
  - [25] N. Nakada, K. Mizutani, T. Tsuchiyama, S. Takaki, Difference in transformation behavior between ferrite and austenite formations in medium manganese steel, *Acta Mater.* 65 (2014) 251–258.
  - [26] M. Koyama, Z. Zhang, M. Wang, D. Ponge, D. Raabe, K. Tsuzaki, H. Noguchi, C.C. Tasan, Bone-like crack resistance in hierarchical metastable nanolaminate steels, *Science* 355 (6329) (2017) 1055–1057.
  - [27] M.M. Wang, C.C. Tasan, D. Ponge, A. Kostka, D. Raabe, Smaller is less stable: size effects on twinning vs. transformation of reverted austenite in TRIP-maraging steels, *Acta Mater.* 79 (2014) 268–281.
  - [28] M.M. Wang, C.C. Tasan, D. Ponge, A.C. Dippel, D. Raabe, Nanolaminate transformation-induced plasticity–twinning-induced plasticity steel with dynamic strain partitioning and enhanced damage resistance, *Acta Mater.* 85 (2015) 216–228.
  - [29] M. Kuzmina, M. Herbig, D. Ponge, S. Sandlöbes, D. Raabe, Linear complexes: confined chemical and structural states at dislocations, *Science* 349 (2015) 1080–1083.
  - [30] F. Moszner, E. Povoden-Karadeniz, S. Pogatscher, P.J. Uggowitzer, Y. Estrin, S.S.A. Gerstl, E. Kozeschnik, J.F. Löffler, Reverse  $\alpha' \rightarrow \gamma$  transformation mechanisms of martensitic Fe-Mn and age-hardenable Fe-Mn-Pd alloy upon fast and slow continuous heating, *Acta Mater.* 72 (2014) 99–109.
  - [31] R. Kapoor, L. Kumar, I.S. Batra, A dilatometric study of the continuous heating transformation in 18wt.%Ni maraging steel of grade 350, *Mater. Sci. Eng.*, A 352 (1–2) (2003) 318–324.
  - [32] R. Kapoor, I.S. Batra, On the  $\alpha'$  to  $\gamma$  transformation in maraging (grade 350), PH 13-8 Mo and 17-4 PH steels, *Mater. Sci. Eng. A* 371 (2004) 324–334.
  - [33] M. Kuzmina, D. Ponge, D. Raabe, Grain boundary segregation engineering and austenite reversion turn embrittlement into toughness: example of a 9 wt.% medium steel, *Acta Mater.* 86 (2015) 182–192.
  - [34] A. Kwiatkowski da Silva, G. Leysin, M. Kuzmina, D. Ponge, M. Herbig, S. Sandlöbes, B. Gault, J. Neugebauer, D. Raabe, Confined chemical and structural states at dislocations in Fe-9wt%Mn steels: a correlative TEM-atom probe study combined with multiscale modelling, *Acta Mater.* 124 (2017) 305–315.
  - [35] A. Kwiatkowski da Silva, G. Inden, A. Kumar, D. Ponge, B. Gault, D. Raabe, Competition between formation of carbides and reversed austenite during tempering of a medium-manganese steel studied by thermodynamic-kinetic simulations and atom probe tomography, *Acta Mater.* 147 (2018) 165–175.
  - [36] P. Dastur, A. Zarei-Hanzaki, R. Rahimi, V. Klemm, B. De Cooman, J. Mola, Nanoscale partitioning of Mn between austenite and martensite revealed by Curie temperature variations, *Phil. Mag. Lett.* (2018), <https://doi.org/10.1080/09500839.2018.1465238>.
  - [37] W.M. Huang, An assessment of the Fe-Mn system, *Calphad Comput. Coupling Phase Diagrams Thermochem.* 13 (3) (1989) 243–252.
  - [38] D. Djurovic, B. Hallstedt, J. von Appen, R. Dronskowski, Thermodynamic assessment of the Mn-C system, *Calphad Comput. Coupling Phase Diagrams Thermochem.* 34 (3) (2010) 279–285.
  - [39] D. Djurovic, B. Hallstedt, J. von Appen, R. Dronskowski, Thermodynamic assessment of the Fe-Mn-C system, *Calphad Comput. Coupling Phase Diagrams Thermochem.* 35 (4) (2011) 479–491.
  - [40] G. Inden, P. Neumann, Simulation of diffusion-controlled phase transformations in steels, *Steel Res.* 67 (1996) 401–407.
  - [41] A. Borgenstam, L. Höglund, J. Ågren, A. Engström, DICTRA, a tool for simulation of diffusional transformations in alloys, *J. Phase Equil.* 21 (3) (2000) 269–280.
  - [42] A. Schneider, G. Inden, Simulation of the kinetics of precipitation reactions in ferritic steels, *Acta Mater.* 53 (2) (2005) 519–531.
  - [43] K. Thompson, D. Lawrence, D.J. Larson, J.D. Olson, T.F. Kelly, B. Gorman, In situ site-specific specimen preparation for atom probe tomography, *Ultramicroscopy* 107 (2–3) (2007) 131–139.
  - [44] B.P. Geiser, D.J. Larson, E. Oltman, S. Gerstl, D. Reinhard, T.F. Kelly, T.J. Prosa, Wide-field-of-view atom probe reconstruction, *Microsc. Microanal.* 15 (2009) 292–293.
  - [45] I.R. Souza Filho, M.J.R. Sandim, R. Cohen, L.C.M. Nagamine, H.R.Z. Sandim, D. Raabe, Magnetic properties of a 17.6Mn-TRIP steel: study of strain-induced martensite formation, austenite reversion, and athermal  $\alpha'$ -formation, *J. Magn. Magn. Mater.* 473 (2019) 109–118.
  - [46] C. García de Andrés, F.G. Caballero, C. Capdevila, L.F. Álvarez, Application of dilatometric analysis to the study of solid-solid phase transformations in steels, *Mater. Char.* 48 (2002) 101–111.
  - [47] Y. Lü, B. Hutchinson, D.A. Molodov, G. Gottstein, Effect of deformation and annealing on the formation and reversion of  $\epsilon$ -martensite in an Fe–Mn–C alloy, *Acta Mater.* 58 (2010) 3079–3090.
  - [48] B.D. Cullity, C.D. Graham, *Introduction to Magnetic Materials*, second ed., John Wiley and Sons, New Jersey, 2009.
  - [49] B.H. Jiang, Limin Sun, Ruchun Li, T.Y. Hsu (Xu Zuyao), Influence of austenite grain size on  $\gamma \rightarrow \epsilon$  martensitic transformation temperature in Fe-Mn-Si-Cr alloys, *Sci. Metall. Mater.* 33 (1) (1995) 63–68.
  - [50] B.H. Jiang, Xuan Qi, Weiming Zhou, T.Y. Hsu (Xu Zuyao), Comment on “Influence of austenite grain size on  $\gamma \rightarrow \epsilon$  martensitic transformation temperature in Fe-Mn-Si-Cr alloys”, *Scripta Mater.* 34 (5) (1996) 771–773.
  - [51] J.B. Seol, D. Raabe, P.P. Choi, Y.R. Im, C.G. Park, Atomic scale effects of alloying, partitioning, solute drag and austempering on the mechanical properties of high-carbon bainitic–austenitic TRIP steels, *Acta Mater.* 60 (2012) 6183–6199.
  - [52] M.K. Miller, D.W. Smith, An atom probe study of the anomalous field evaporation of alloys containing silicon, *J. Vac. Sci. Technol.* 19 (1981) 57–62.
  - [53] Y.C. Liu, F. Sommer, E.J. Mittemeijer, Abnormal austenite-ferrite transformation behaviour in substitutional Fe-based alloys, *Acta Mater.* 51 (2) (2003) 507–519.
  - [54] H.I. Aaronson, M. Enomoto, J.K. Lee, *Mechanisms of Diffusional Phase Transformations in Metals and Alloys*, CRC Press, Boca Raton, FL, 2010.
  - [55] M. Hillert, in: H.I. Aaronson (Ed.), *Lectures on the Theory of Phase Transformations*, second ed., TMS-AIME, Warrendale, PA, 1975, p. 1, 1999, p. 1.
  - [56] D.A. Porter, K.E. Easterling, M.Y. Sherif, *Phase Transformations in Metals and Alloys*, CRC Press, Boca Raton, FL, 2009.
  - [57] A. Kwiatkowski da Silva, D. Ponge, Z. Peng, G. Inden, Y. Lu, A. Breen, B. Gault, D. Raabe, Phase nucleation through confined spinodal fluctuations at crystal defects evidenced in Fe-Mn alloys, *Nat. Commun.* 9 (2018) 1137.